

Centrifuge modelling of submarine landslides due to static liquefaction

Zhang, Weiyuan; Askarinejad, Amin

DOI

[10.1007/s10346-019-01200-z](https://doi.org/10.1007/s10346-019-01200-z)

Publication date

2019

Document Version

Final published version

Published in

Landslides

Citation (APA)

Zhang, W., & Askarinejad, A. (2019). Centrifuge modelling of submarine landslides due to static liquefaction. *Landslides*, 16(10), 1921-1938. <https://doi.org/10.1007/s10346-019-01200-z>

Important note

To cite this publication, please use the final published version (if applicable). Please check the document version above.

Copyright

Other than for strictly personal use, it is not permitted to download, forward or distribute the text or part of it, without the consent of the author(s) and/or copyright holder(s), unless the work is under an open content license such as Creative Commons.

Takedown policy

Please contact us and provide details if you believe this document breaches copyrights. We will remove access to the work immediately and investigate your claim.

Centrifuge modelling of submarine landslides due to static liquefaction

Abstract Sand erosion and scouring caused by waves and marine currents result in gradual increase of local seabed inclination and formation of slopes around hydraulic structures and offshore foundations. During this process, shear stresses in the soil body increase monotonically which may lead to static liquefaction and damage of the adjacent offshore infrastructure. This paper presents the details of a newly developed static liquefaction triggering actuator to be used at an enhanced gravity condition in a geotechnical centrifuge. This actuator simulates the steepening process of submarine sand layers due to scouring and enables the investigation of failure mechanisms in submerged slopes. The details of the centrifuge test set-up designed and constructed to simulate the process of triggering static liquefaction in loose sand layers are presented. Furthermore, the performance of the novel integrated model preparation facility using sand fluidization is explained. The set-up was used to conduct several centrifuge tests at four different slope steepening rates to investigate the slope steepening rate effects. Moreover, the effect of viscosity of the submerging pore fluid on the behaviour of the slopes at the onset of failure is investigated. The Coriolis effect on loose saturated sand samples during increase of g-level is examined as well. Results show that the built-up of pore pressure due to local shear deformations can be detected and considered as one of the triggering mechanisms of this kind of submarine slope instabilities.

Keywords Submarine landslides · Static liquefaction · Centrifuge modelling · Offshore foundations

Introduction

The failure of natural or man-made slopes under water is one of the main threats to offshore assets. Liquefied submerged slopes or embankments are often characterized by relatively small failure angle, sudden failure, a considerable amount of released soil mass and large influencing areas (Kvalstad et al. 2001). These make static liquefaction to be one of the most catastrophic mechanisms of under-water slope failures. Instability of these slopes can be triggered by static loads, such as sediments deposition, toe erosion, rising of an embankment height, scours near a structure or dredging activities (Kvalstad et al. 2001; Wanatowski and Chu 2012; Sadrekarimi 2016; De Jager 2017; Maghsoudloo 2017). Several cases of static liquefaction of submarine slopes and flow slides have been reported in the literature (Andresen and Bjerrum 1967; Bjerrum 1971; Sladen et al. 1985b; Kramer 1988; Kraft Jr et al. 1992). Numerous submerged slope instabilities have occurred in Zeeland, the Netherlands, over the past 200 years which were major threats for the flood defence systems (Silvis and Md 1995). Take the case of Eastern Scheldt storm surge barrier as example (Silvis and Md 1995), due to waves and currents scouring happens near the structures as illustrated in Fig. 1, which schematically shows the development of scour hole. During the scouring process, slope inclination increases before reaching a stable condition, which results in change of stress state, leading to an unstable stress

path and liquefaction, as shown in Fig. 1b. Before the scouring occurs, the stress state of the soil element in Fig. 1a is indicated as point A which lies on the K_0 line, where K_0 is the ratio of effective horizontal stress to effective vertical stress at rest. Then, as the scour hole develops and seabed slope angle (θ) rises gradually, mean effective stress (p') decreases while deviator stress (q) increases monotonically under drained condition. Hence, the stress state constantly shifts to upper left in the p' - q space. At a certain point, due to collapse of voids in the soil structure, instability under undrained condition would be triggered when the stress path hits on the instability line (IL) at point B. As a result, excess pore pressure would be generated and the sand would lose its strength suddenly which is expressed as curve BC which lies in between IL and the critical state line (CSL). Full liquefaction happens at point C. Therefore, understanding of soil behaviour and excess pore pressure generation during the increasing of slope inclination is necessary in assessing the failure mechanism of static load-induced liquefaction for marine slopes.

Static liquefaction can occur in a loosely packed sand element under a slight change in the static load, due to the successive micro-collapses of the voids resulting in build-up of pore water pressure in a temporary undrained condition (Sladen et al. 1985a; Lade 1992; Take et al. 2004; Lade and Yamamuro 2011; Askarinejad et al. 2014). Physical modelling techniques (large-/small-scaled models and centrifuge tests) have been applied to study under-water landslide failure behaviour, as they have the advantage of evaluating some specific features of prototypes (Wood 2014). In many large-/small-scaled tests (1g tests), “releasing gate” method was adopted as the slope failure triggering mechanism to investigate the landslide post-failure behaviour. For example, De Groot et al. (2012) and De Groot et al. (2019) summarized a series of static liquefaction experiments in large- and medium-sized flumes. In the large flume, the valid length of samples was 24 m and the height varied from 1.0 to 2.1 m. The samples were kept in position by a rotatable gate which would be lifted with a speed of around 0.1 m/s during the tests. In their medium-sized flume, samples' lengths were about 5.0 and 10.0 m for coarse sand and fine sand, respectively, and their heights were around 0.63 m. By means of dredging, these samples were made with steep slope angles which were kept stable by applying suction from the base. Failures were induced by releasing the suction. Sudden development of excess pore pressures was observed at the onset of slope instabilities in these tests. Spence and Guymer (1997) adopted a similar idea to trigger flow slides. Samples were made on an inclined tank and were kept stable by a watertight barrier before testing. Flow slides were triggered by quickly removing the barrier. A retrogressive non-circular slipping behaviour of flow side motion was observed. Ilstad et al. (2004) studied subaqueous debris flows in a 10-m long tank. The clay-sand mixture was stored in a reservoir which was hanging above a 6° rough bed. By releasing the gate of the reservoir, debris could flow down along the bed during which the pore pressure evolution was recorded.

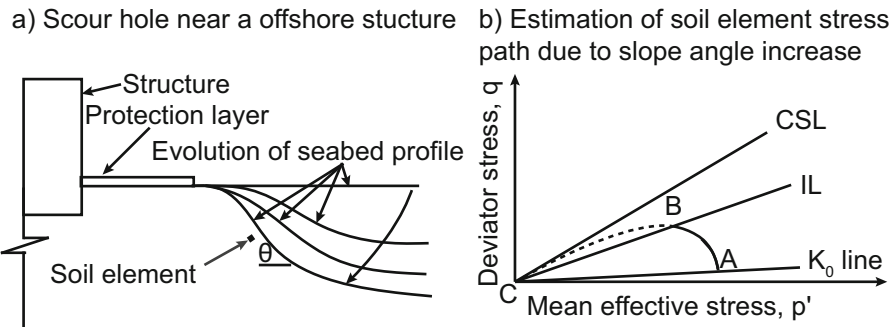


Fig. 1 Schematic view of development of seabed inclination due to scouring and resultant effective stress path

Similarly, Yamada et al. (2010) conducted several sandbox analogous experiments using dry sand to study submarine landslides triggered by slope steepening due to tectonic deformation. However, this test model is unable to consider the built-up of pore water pressure. Alternatively Byrne et al. (2000) built an 8-m high clay embankment with a slope angle of 21.8° over a loose saturated sand layer in the field as part of the Canadian Liquefaction Experiment project. The intent of this field test was to trigger liquefaction in the loose sand layer by applying static load rapidly; however, the embankment was stable during the event. They concluded that the direction of loading, which controls the soil residual strength, and the drainage conditions governed the stability of the base sand layer. De Jager (2018) designed a large-scale 1g liquefaction tank at TU Delft with the main purpose of investigating slope over-steepening effects on under-water liquefaction. Submerged fine sand samples were prepared flat initially and then were triggered to failure by lifting up one side of the 1g liquefaction tank constantly and slowly. He found that slope failure is governed by the looser part of the sample and tilting rate affects slope instability. However, the maximum sand layer height is 1.5 m, and the maximum tilting angle is 10° in this facility. The application of 1g tests' results to field situation is restricted by the model-scale effects.

Simulation of in situ stress conditions is vital for the assessment of soil strength, soil resistance to liquefaction and pore pressure conditions (Schofield 1980; Kvalstad et al. 2001). Centrifuge technique has the advantage of preserving the stress condition in the field in a small-scaled model at a high centrifugal acceleration condition and has been widely applied in geotechnical engineering. The "releasing gate" method, adopted in the 1g tests performed by De Groot et al. (2012), De Groot et al. (2019), Spence and Guymer (1997) and Ilstad et al. (2004), has been applied into centrifuge modelling for studying the landslide flow behaviour as well (e.g. Boylan et al. 2010; Gue et al. 2010; Acosta et al. 2017; Yin et al. 2017). However, only clay/slurry materials have been used in these models. It has been acknowledged that application of "releasing gate" method is capable of providing useful information about flow slide behaviour which is assumed to be independent of initiation method (Spence and Guymer 1997).

However, knowing the potential triggering mechanisms of marine landslides is of crucial importance in order to reduce the chance of seabed liquefaction during construction and the whole lifetime of offshore structures, such as pipelines, wind turbine foundations and barriers. Several marine landslides triggering

mechanisms were investigated in centrifuge, such as earthquake-induced landslides (e.g. Coulter and Phillips 2003; Elgamal et al. 2005) and wave-induced landslides (e.g. Sassa and Sekiguchi 1999). However, only few centrifuge experiments have been conducted on fully saturated soil under static loading condition. One of the first reported static liquefaction tests conducted in centrifuge was done by Phillips and Byrne (1995). As a result of dropping a surcharge above the slope crest, liquefaction was induced and the slope angle changed from 16° to 7° after failure. Zhang et al. (2015) studied the generation of high pore pressure in gentle submarine slopes. Samples were composed of a layer of kaolin clay on the top and a thin sand layer below. Slope failures were triggered in flight by injecting pore fluid into the sand layer from the embedded perforated pipes. Accumulation of pore pressure was observed before the major failure. Zhang et al. (2015) used saline water to simulate seawater, whereas the scaling effect of pore fluid was not considered. Based on literature study, effects of the increasing of submarine slope inclination on the slope instability have not been studied in centrifuge yet.

The objective of this paper is to introduce a new geotechnical centrifuge testing facility which is designed to investigate the static liquefaction mechanism in submarine sandy slopes. Due to the special requirements for conducting centrifuge tests on very loose saturated sand samples, a new strongbox equipped with a fluidization system was developed. In this paper, the details of the testing facility are presented. Furthermore, the sample properties, such as uniformity, distribution of relative density and degree of saturation across the sample, are discussed. Besides, the development of excess pore pressure inside the soil layer prior to and post failure is analysed.

Sample preparation

Sample preparation methods affect soil structure, saturation, uniformity and relative density and therefore have a major influence on the sample behaviour (Vaid et al. 1999; Della et al. 2011). Kramer (1988) compared several historical liquefaction flow slides that happened in coastal areas, such as the slow slides which occurred in Orkdalsfjord of Norway in 1930, and found that the natural deposit materials are similar in these areas which are described as silty fine sand or loose fine sand. Modelling the depositional process is essential for resembling prototype soil structure and for assessment of the generation of excess pore pressure (Kvalstad et al. 2001). Therefore, the sample prepared for the physical

modelling should have similar properties to that in the field for simulating slope static liquefaction. Furthermore, a special design is required for transporting the sample from the preparation area to the carrier of the geo-centrifuge. Since a small disturbance could cause sample densification. In this section, we discuss about the various conventional sample preparation methods and explain the details of a strongbox designed for making samples as well as the soil and pore fluid material used in this study.

Background

Coulter and Phillips (2003) prepared fully saturated sand samples for studying earthquake effects on soil liquefaction in centrifuge. Sand samples with relative densities of 38–42% were made by a combination of air pluviation technique, sample saturation technique (using vacuum and carbon dioxide) and pore fluid replacing technique. Rietdijk et al. (2010) developed the drizzle method for creating saturated samples with Dr around 5%. However, such a loose sample would be densified in the process of sample transportation. Askarinejad et al. (2018) adopted the water pluviation method and successfully prepared saturated slopes with relative density of 15%. However, this technique was reported to be extremely time consuming, i.e. approximately 8 h was required to construct a sample in a strongbox with dimensions of 270 mm × 150 mm × 135 mm.

Fluidization technique has been applied in physical modelling as the sample preparation technique to simulate the formation of a seabed/riverbed in coastal areas (Spence and Guymer 1997; De Groot et al. 2012; De Jager 2018). The fluidization technique has the following three advantages: (i) the sample properties are reproducible; (ii) the uniformity of samples can be guaranteed; (iii) the achieved average relative density can be as low as that of the prototype. Spence and Guymer (1997) got loose samples with Dr less than 31% by fluidizing sand around 30 min. De Groot et al. (2012) reported that the relative density was discharge-related. The 1g liquefaction tank at TU Delft (De Jager 2018) is equipped with a fluidization system at the base which is composed of a filter and perforated pipes. Samples with relative densities ranging from 28 to 58% were made by adjusting the discharge of the fluidization system.

Fluidization system

A strongbox was constructed for the beam centrifuge at TU Delft with a U-shaped aluminium frame and two transparent side walls made of Plexiglass. The dimensions of the strongbox were designed to take advantage of the space in the centrifuge carrier. Samples with a length of 355 mm, a width of 134 mm and height of up to 110 mm, at model scale, can be prepared (Fig. 2). The pore pressure developments in the soil layer can be monitored by three pore pressure transducers (PPTs, MPXH6400A) during both sample preparation and testing.

A fluidization system was integrated to the base of the strongbox. It is composed of three parts: a filter layer (Fig. 3), a network of perforated pipes system (Fig. 4) and a pump. The filter layer is sandwiched between the sand (on top) and the perforated pipes system (at the bottom). The filter layer has two main functions: (i) to prevent sand particles from blocking the perforated pipes system, and (ii) to allow a smooth and uniform flushing of external fluid into the sand layer. Moreover, the filter layer was designed to be rigid enough to resist the deformation which might be caused by the sand weight during centrifuge spinning. The filter is made

up of three mesh layers: a top mesh which is a fine square hole perforated stainless steel mesh, a bottom mesh which is a coarse round hole perforated stainless steel mesh and a middle mesh which is a fine Nylon mesh filter (Fig. 3). The bottom mesh has an opening size of 3 mm and a thickness of 1 mm, and it is seen as the backbone of the filter layer; the pore size of the Nylon mesh filter is 41 μm which is chosen to be smaller than D_{10} of Geba Sand (Table 1); the top mesh has an opening size of 0.5 mm and a thickness of 0.5 mm which functions as the protection layer for the Nylon mesh filter. The filter layer was fixed onto a 6-mm-thick aluminium frame (Fig. 4), which was mounted on the base of the strongbox through screws; besides, it was supported by four 3-mm thick and evenly distributed PVC sticks as well. The PVC sticks were also used to secure the perforated pipes. A sealing rubber belt was placed in between the filter layer and the aluminium frame for preventing leakage along the boundaries of the filter layer (Fig. 3).

The perforated pipe system is composed of eight parallel pipes with outer diameter of $D_o = 6$ mm and inner diameter of $D_i = 4$ mm which are connected to a transverse pipe with $D_o = 12$ mm and $D_i = 10$ mm (Fig. 4). Fifty openings with diameter of 0.5 mm are evenly distributed along each small pipe. Based on experience of the construction of the 1g liquefaction tank (De Jager 2018), a uniform sand sample requires a uniform fluid pressure in the fluidization system. Considering that the outflow will generate a pressure gradient along each perforated pipe, the rule that the area of outlet should be smaller than or equal to the inlet area is guaranteed, e.g. the total area of the 50 openings on one perforated pipe is smaller than the inner area of the pipe, thus the pressure difference in the pipe remains relative small. The existence of the fine Nylon mesh filter may further unify the fluid pressure in the fluidization system. Moreover, these openings are designed to be facing downwards (Fig. 4). This design is assumed to be useful to improve the uniformity of the fluid pressure below the fluidization filter.

Two inlet valves were connected to the transverse pipe from outside of the strongbox (see further in Fig. 11). These valves were open during the fluidization and closed during the centrifuge tests. Because there are no openings on the transverse pipe, less discharge would be expected in the zone above the transverse pipe which may cause sample non-uniformity. Therefore, a PVC block was fixed onto the filter layer above the area of the transverse pipe (Fig. 2). The submerging fluid height from the sample bottom was 180 mm (model scale) for all tests. A modular four-sided “extension box” on top of the strongbox provides enough space for the submerging fluid and generated waves after the landslides (see further in Fig. 11).

A Grundfos PO07 water pump was used to fluidize the sand. One side of the pump was connected to the two valves (Fig. 11) and the other side was connected to a container filled with de-aired fluid. A third valve was installed in a tube connecting the pump and the strongbox for controlling the discharge. The minimum fluid velocity for fluidizing the sample (V_{mf}) can be estimated based on Eq. 1 proposed by Lowe (1976),

$$V_{mf} = -\frac{150a_2\mu_f}{3.5a_1D_{\text{particle}}\rho_f} + \left[\left(\frac{150a_2\mu_f}{3.5a_1D_{\text{particle}}\rho_f} \right)^2 + \frac{D_{\text{particle}}g(\rho_{\text{particle}} - \rho_f)}{1.75a_1\rho_f} \right]^{1/2} \quad (1)$$

where a_1 and a_2 are suggested to be as 14 and 11, respectively (Wen and Yu 1966); μ_f is kinematic viscosity of the fluidization fluid

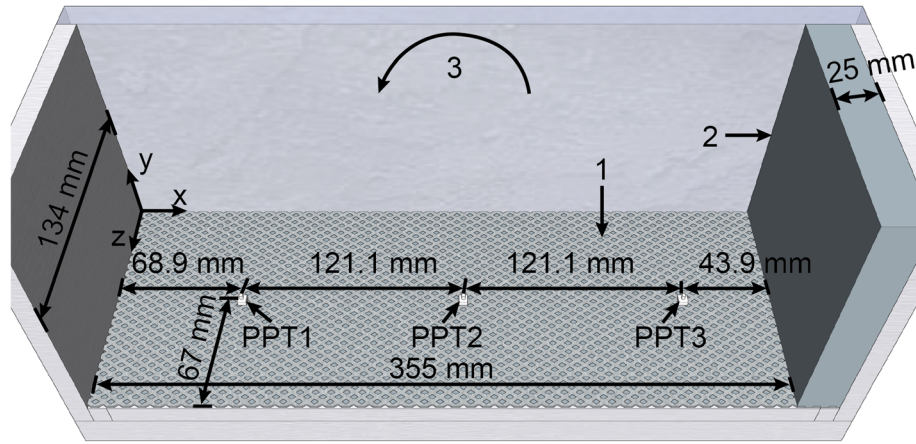


Fig. 2 Fluidization system (outside view, model scale): 1, filter layer; 2, PVC block; 3, tilting direction

($g/cm\ s$); $D_{particle}$ is sand particle diameter (cm); ρ_f and $\rho_{particle}$ are fluidization fluid density and sand particle density (g/cm^3), respectively; g is acceleration due to gravity (cm/s^2). Substituting $\mu_f = 0.01\ g/(cm\ s)$, $D_{particle} = 1.17 \times 10^{-2}\ cm$ ($= D_{50}$ in Table 1), $\rho_{particle} = 2.67\ g/cm^3$ obtained from G_s in Table 1, $\rho_f = 1.0\ g/cm^3$ for de-aired water and $g = 981\ cm/s^2$ into Eq. 1 yields $V_{mf} = 1.36 \times 10^{-4}\ m/s$. The applied discharge was around $1.8 \times 10^{-3}\ m/s$ from the filter of the fluidization mesh when using de-aired water which is larger than the estimated minimum fluid velocity for fluidizing the sample ($V_{mf} = 1.36 \times 10^{-4}\ m/s$). Applying this discharge during sample preparation, the excess pore pressure ratio (r_u) at PPT1 is around 1.0 and r_u at PPT3 is around 0.93. Hence, it is believed that this fluidization system is able to uniformly liquefy sand samples during the process of fluidization.

Soil material

Sub-angular and sub-rounded sand, known as Geba Sand, supplied by Eurogrit (www.eurogrit.com) was used in this study which was also used and characterized by De Jager (2018), Askarinejad et al. (2018) and Maghsoudloo et al. (2018). The soil properties are listed in Table 1, where D_{10} , D_{50} and D_{60} are the intercepts for 10, 50 and 60% of the cumulative mass; $\phi'_{residual}$ is residual friction angle;

K is coefficient of permeability tested with water as the submerging fluid; e means void ratio, and the subscripts min and max denote the minimum and maximum void ratios, respectively; and G_s is sand specific gravity.

Pore fluid

In this study, both de-aired water and de-aired viscous fluid were used. Hydroxypropyl methylcellulose (HPMC) powder is biodegradable and can dissolve in water easily. Viscous fluid made of HPMC has been widely used in centrifuge modelling considering the difference in the scaled time for the pore fluid generation and dissipation under Ng condition (N times Earth's gravity, g). Dewoolkar et al. (1999) and Ko (1994) argued that the soil constitutive properties will not be changed by HPMC solutions. Stewart et al. (1998) reported that for a concentration of 2% for HPMC, the solution has a density of no more than 0.5% higher than water. Therefore, HPMC powder marketed as Benecel E10M supported by ASHLAND was used in this research.

The employed dispersion method was the "hot/cold" technique (The Dow Chemical Company 2002). The de-aired viscous fluid was made by the following steps: i. approximately 20% of the required volume of water was heated to around 90 °C; ii. the

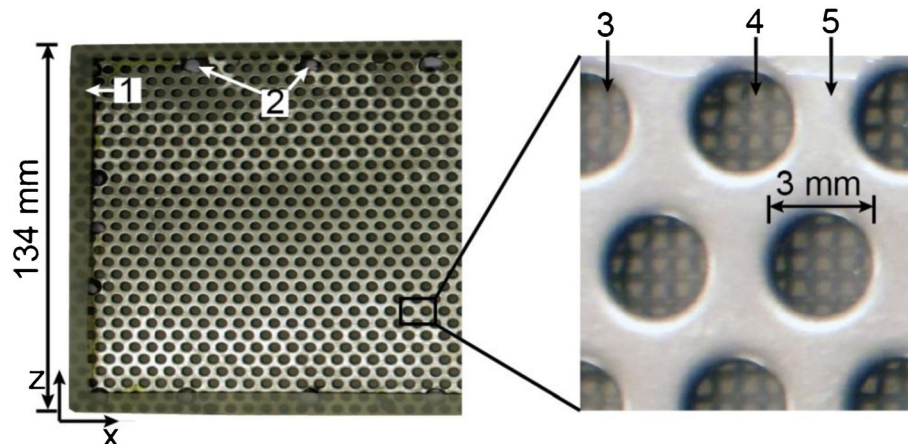


Fig. 3 Filter layer of fluidization system (model scale): 1, sealing rubber; 2, screw holes; 3, top mesh; 4, middle filter; 5, bottom mesh

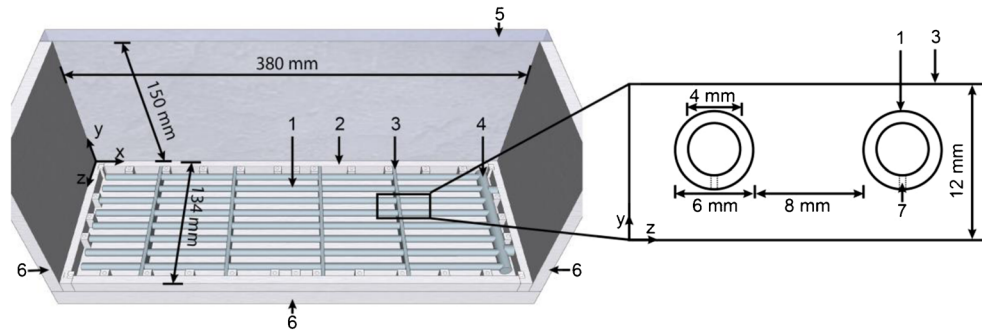


Fig. 4 Fluidization system (inside view, model scale): 1, parallel pipes; 2, aluminium frame; 3, PVC sticks; 4, transverse pipe; 5, Plexiglas; 6, U-shape frame; 7, openings with diameter of 0.5 mm

HPMC powder was mixed into the warm water in a blender; iii. agitation was continued until the powder was evenly dispersed; iv. the prepared fluid was mixed into the rest of required water; v. the viscous fluid was de-aired by vacuum for at least 12 h.

Sample preparation procedures at 1g condition

The sand mixed with de-aired fluid was put into a vacuum for 24 h. It was carefully transported into the strongbox which had been filled with de-aired fluid already to avoid any air bubbles. In order to prepare samples easily and in a reproducible manner, the procedures listed in Appendix A were repeated for every centrifuge test. The pore pressure change recorded during the sample preparation for all the samples are similar which confirms the reproducibility of the fluidization technique. The fluid was put under vacuum for at least 12 h after every two tests.

There are four main advantages for this sample preparation technique. Firstly, the sample preparation time is no more than 40 min which is far less compared to the 8 h per sample by the wet pluviation method (Askarnejad et al. 2018); secondly, each sample can be made in the centrifuge carrier which excludes any possible artificial disturbance before starting the centrifuge; thirdly, no extra space above the strongbox on the centrifuge carrier is needed for preparing a sample; hence, the vertical space of centrifuge carrier can be fully utilized; lastly, since the same procedures are followed for every test, the reproducibility, fully saturated condition and loose state of the sand samples are ensured. These qualities are discussed in the following section.

Sample properties

Relative density

The average sand layer height of each test was obtained from five scales which were attached on inside of the Plexiglas walls of the strongbox at different positions (two of them can be seen in Fig. 11 and the rest of scales were attached onto the other Plexiglas wall) at 1g condition and from two scales (see Fig. 11 and Fig. 14) at Ng

condition. The initial relative densities at 1g condition (Dr_{1g}) and relative densities at Ng condition (Dr_{Ng}) are listed in Table 2, where N is 10 in this study. As a result of rise of centrifugal acceleration, the samples became denser.

Degree of saturation

Submerged sand samples were kept under vacuum for more than 24 h before being transferred into the strongbox. The sand column method (Chapuis 2004) was adopted to examine the degree of saturation (S_r) of sand layer after fluidization. Results are presented in Table 3. The prepared de-aired viscous fluid was put under vacuum after every two tests.

Uniformity

Petrovic et al. (1982) concluded that computed tomography (CT) scanning is a useful technique to evaluate soil bulk density. The homogeneity (Table 2) in terms of relative density was investigated by scanning a sample using a Siemens Somatom Volume Zoom CT scanner with a maximum resolution of 0.6 mm. This CT scanner is capable of generating 24 sequential images for a layer with thickness of 27 mm in a single scan. Thus, each image has a thickness of 1.25 mm. Each pixel of the images has a size of $0.59 \times 0.59 \text{ mm}^2$. The voltage and current were set at 120 kV and 35 mA, respectively.

A loose soil sample was made following the same preparation procedures as that applied for other samples listed in Table 2. This sample was prepared directly on the CT scanner table so that the sample was intact before scanning. The same sand and de-aired water was used. The influence of fluid viscosity on the samples' homogeneity is considered to be insignificant as all the tested samples were fully fluidized and consolidated at 1g condition. Therefore, the soil properties of this sample are assumed to be similar to that of centrifuge test samples. The computed tomography number (CT_{number}) is expressed in Hounsfield Units (HU) and is proportional to the densities of scanned materials. Figure 5 illustrates 3D view of the strongbox in HU in greyscale. In Fig. 5 and following figures which are shown in HU, a material with

Table 1 Main sand properties (after Maghsoudloo 2017; Maghsoudloo et al. 2018)

D_{10} (mm)	D_{50} (mm)	D_{60} (mm)	ϕ'_{residual} ($^{\circ}$)	K (m/s)	e_{min}	e_{max}	G_s
0.078	0.117	0.121	36	4.2×10^{-5} or 1.3×10^{-5a}	0.64	1.07	2.67

^aTheoretical value when the submerging fluid has a viscosity of 3.2 cSt

Table 2 Summary of centrifuge tests

Test name ^a	Tilting rate (°/s) Model scale	Prototype scale	g-level (N)	Dr_{1g} (%)	Dr_{Ng} (%)	Height (m, prototype scale)	Failure angle, θ_f (°)
W_0.01_10g	0.1	0.01	10	28	43	1.07	–
W_0.1_10g	1.0	0.1	10	35	49	1.07	–
W_0.2_10g	2.0	0.2	10	20	32	0.74	13.4
V_0.01_10g_NoSand	0.1	0.01	10	–	–	–	–
V_0.01_10g	0.1	0.01	10	23	35	0.83	17.7
V_0.05_10g	0.5	0.05	10	27	37	0.86	12.2
V_0.1_10g	1.0	0.1	10	31	42	0.83	11.1
V_0.2_10g	2.0	0.2	10	27	43	0.88	9.0

^a W stands for de-aired water; V stands for viscous fluid; the number after W or V stands for the testing tilting rate at prototype scale in [°/s]; 10g represents the testing g-level; NoSand means the test was done with viscous fluid only and no sand

higher density is presented brighter than a material with a lower density. For example, in Fig. 5, the density of the aluminium frame of the strongbox (number 8) is higher than that of submerged sand (number 4) which is higher than that of submerging fluid (number 3); hence, number 8 is the brightest and number 3 has the lowest brightness among these three materials. The air has the lowest density in the system; therefore, it is shown in black in these images. With assumption of full saturation, the sand sample can be considered as a porous medium with two phases.

Calibration of CT results

The CT_{number} is proportional to scanned material density when the voltage of the CT scanner is larger than 100 kV (Higo et al. 2011; Gupta et al. 2018). Based on the CT_{number} for air, water, Plexiglas and aluminium which have densities of 0.0012, 1, 1.19 and 2.7 g/cm³, respectively, the CT scanner was calibrated as shown in Fig. 6. The bulk density of saturated sand material can be expressed in Eq. 2, ρ_f is submerging fluid density which is 1 g/cm³ in this study. Thus, sample void ratio can be obtained from CT_{number} based on Eq. 3, where $a_1 = 0.0010$ and $a_2 = 1.0146$ are two parameters determined after calibrating CT_{number} .

$$\text{Bulk density} = \frac{G_s + e\rho_f}{1 + e} \quad (2)$$

$$e = \frac{G_s - 1}{a_1 CT_{\text{number}} + a_2 - 1} - 1 \quad (3)$$

Beam hardening correction method

Due to the difference in densities of the submerged sand and the stainless steel (filter layer), there are beam hardening artefacts

existing in the sample especially in the zone close to the filter layer. A large unexpected variation in CT_{number} was observed. Application of advanced and complicated beam hardening correction (BHC) algorithms, such as the algorithms proposed by Kyriakou et al. (2010) and Gu and Dogandžić (2016), is out of scope of this study; hence, a simple way of correcting beam hardening was adopted. According to the maximum and minimum void ratios (Table 1) and Eq. 3, the largest and lowest expected CT_{number} can be obtained which are 975.4 (HU) and 760.1 (HU). Thus, every CT_{number} which either exceeds 965.7 (HU) or lower than 760.1 (HU) is deleted.

Relative density distribution along sample height, width and length

It should be noted that due to the setting of the CT scanner, only a slice of sample with a thickness around 30 mm in length direction, i.e. x direction, could be scanned still as shown in Fig. 5; then, the scanner table carrying the strongbox had to be moved in order to scan the whole sample in x direction. However, due to the movement of the scanner table, the sample was disturbed. Hence, only relative density distributions over sample width and depth could be obtained from undisturbed sample (Fig. 7a); relative density distribution over sample length could be only evaluated based on the same sample which was partially disturbed as illustrated in Fig. 7b.

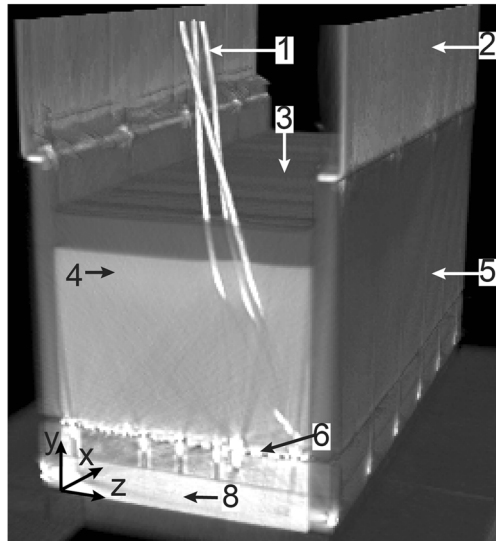
Figure 7a demonstrates the 2D view of cross section of the sample (around 27 mm in out-of-plane direction, i.e. x direction). The whole sand sample cross section (90 × 134 mm²) was used to analyse the relative density distribution over sample depth and width. Dr along the sample depth is illustrated in Fig. 8. By comparing with the results before and after BHC, it can be seen that the beam hardening artefacts exist and go severely from depth 60 mm to sample bottom and a large amount of beam hardening artefacts can be corrected by the BHC method.

Results after BHC shows that the relative density profile over sample depth is characterized by a looser top layer (0–10 mm), a

Table 3 Degree of saturation measured from four samples after fluidization

	Sample 1	Sample 2	Sample 3	Sample 4	Average
S_r (%)	99.9 ± 1.8	98.7 ± 1.7	98.7 ± 1.6	99.2 ± 1.7	99.1 ± 1.7

a strong box



b cross section

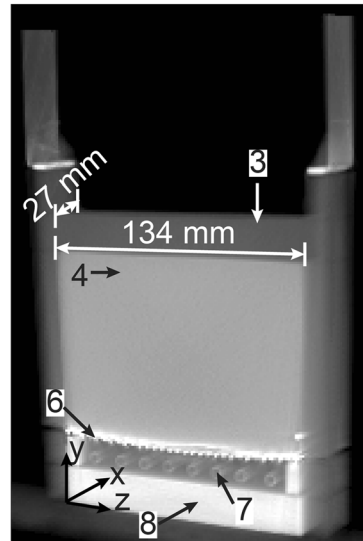


Fig. 5 3D view of the strongbox in Hounsfield Units in greyscale (model scale): 1, cables of PPT; 2, extension box; 3, submerging fluid (de-aired water); 4, submerged sand; 5, Plexiglas; 6, filter layer; 7, parallel fluidization pipes; 8, base of the U-shape aluminium frame of the strongbox

denser bottom layer (70–90 mm) and a relative constant value in between (Fig. 8). It is reasonable that the sample bottom layer is denser than the sand above, as the vertical effect stress increases with the sample depth. However, there might be still some beam hardening artefacts in the bottom layer (from 70 to 90 mm), considering the fact that the effortless BHC method applied in this study is simplistic. The Dr profile over sample width is uniform from 7 to 124 mm (Fig. 9). The relative low Dr near the two sides

might be a consequence of the wall friction effect during sand sedimentation. It can be concluded that the main sample is reasonably uniform in the cross-section plane. The average relative densities over depth and width are around 30.8 and 30.4%, respectively.

Dr profile in the length direction for the sample that was affected by the movement of CT scanner table shows that the top 50 mm sand was densified; however, below 50 mm the sand

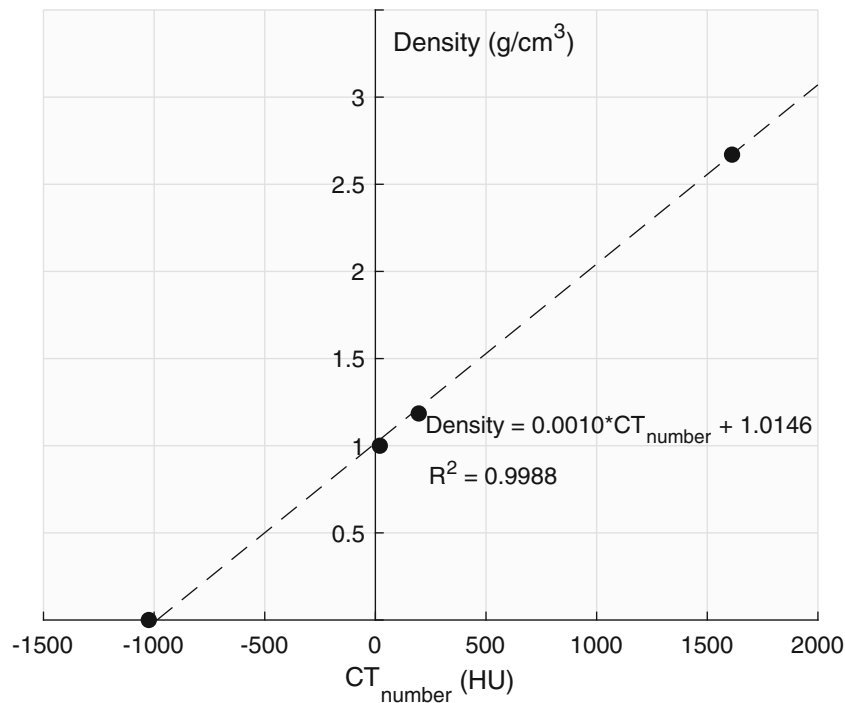


Fig. 6 Calibration of CT_{number}

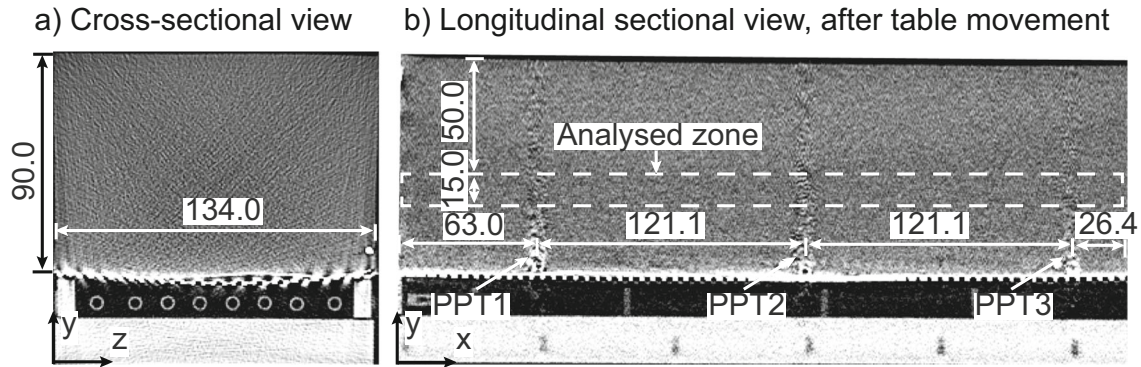


Fig. 7 2D view of the sample in Hounsfield Units in greyscale (model scale): **a** cross-sectional view scanned before the table movement used for analysing D_r distribution along width and depth; **b** longitudinal sectional view scanned after the table movement and the analysed zone is used for analysing D_r distribution along sample length

remained nearly unaffected (Fig. 8). The top 10 mm of the sample was looser than the sand below; hence, this part of sand was prone to densification. However, a 50-mm depth of sand was densified. This might be due to that the disturbance was strong enough to densify the sample more than the top 10-mm layer and the densification of this layer may further influence the sand below due to the dissipation of pore pressure that was expected to be generated. Therefore, not the whole sample but only the analysed zone, in Fig. 7b, which was selected to be within the sample depth from 50 to 70 mm, was used to obtain the D_r distribution over sample length. The analysed zone is assumed to be less affected by the movement of the scanner table and beam hardening effects from the filter. D_r along the sample length is presented in Fig. 10. The existence of PPTs might influence the D_r above them and beam hardening artefacts caused by the sensors might be not corrected completely. Considering the D_r in sample length, it is believed that the sample

is uniform in this direction as well. The average relative density over length is about 29.6%.

Submarine landslide triggering mechanism

A single-plane rotatable set-up was designed to study static liquefaction of submarine slopes induced by the slope over-steepening as a result of the scouring effect (De Groot et al. 2012) or dredging activities. The overview of this set-up is shown in Fig. 11. The base plate, supporting the strongbox, is connected to the 40-mm rotating axis with five bearing blocks. The set-up can rotate using a linear motor (Linak 282100-40150100; capacity, 1 kN). Six shaft blocks connect the casing of the rotating axis to the centrifuge carrier. The outer frame, which consists of four angled profiles at four corners and a lid plate on the top, keeps the strongbox in place and prevents sliding during tilting. A potentiometer (S13FLP25A) linking the base plate and the centrifuge carrier is

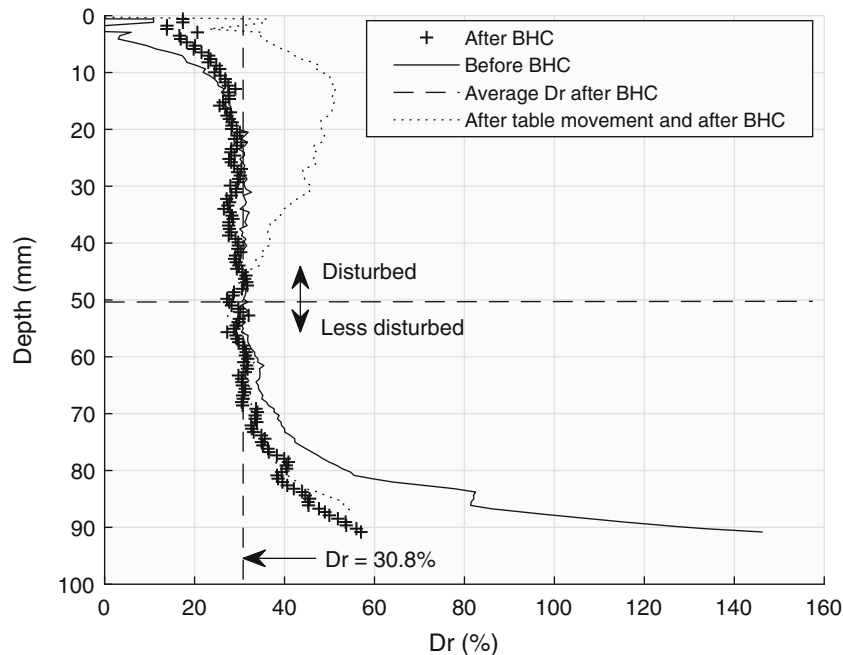


Fig. 8 Variation of relative density over depth (model scale)

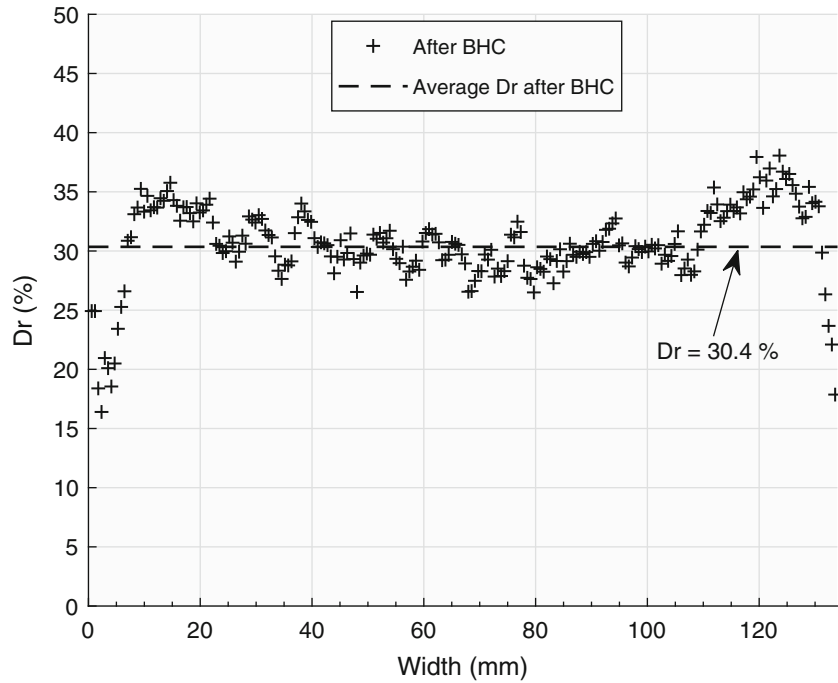


Fig. 9 Variation of relative density over width (model scale)

used to measure the tilting angle. For safety reasons, in case of excessive tilting, two end switches were installed. Metal components of the set-up are made of (7075 aluminium sheet) and designed to be as light as possible.

The weight of the sample is mainly carried by the casing of the rotating axis below the middle of the strongbox; therefore, this

structure of the set-up requires a low capacity for the linear motor. Furthermore, a smooth and linear change of load acting on the linear motor during tilting is expected. The set-up can bear a maximum static load of 47 kN. The maximum tilting angle is 20°. By controlling the linear motor, the strongbox can rotate with a tilting rate (*TR*) ranging from 0.1 to 2.0 %/s with a precision of

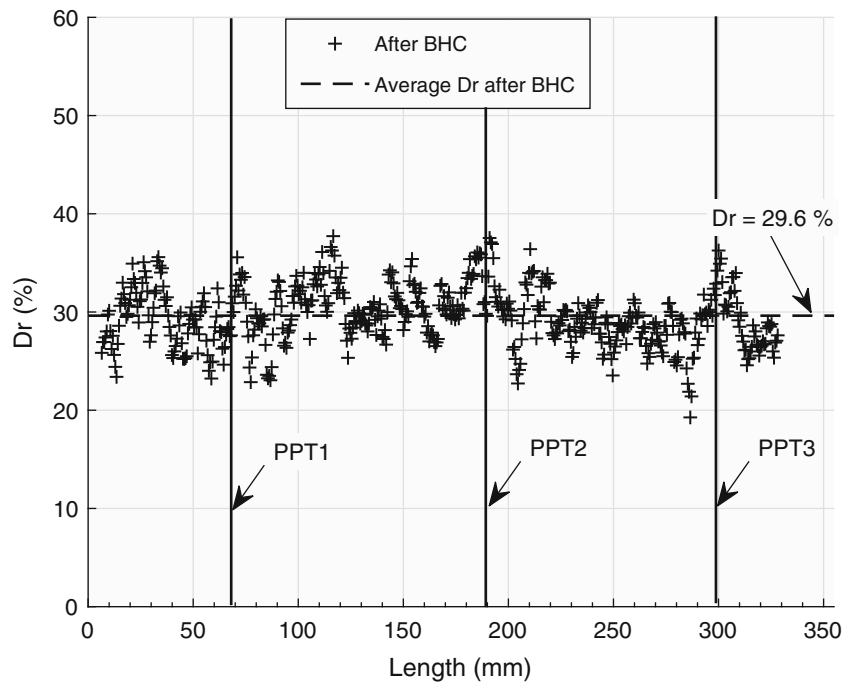


Fig. 10 Variation of relative density over length (model scale)

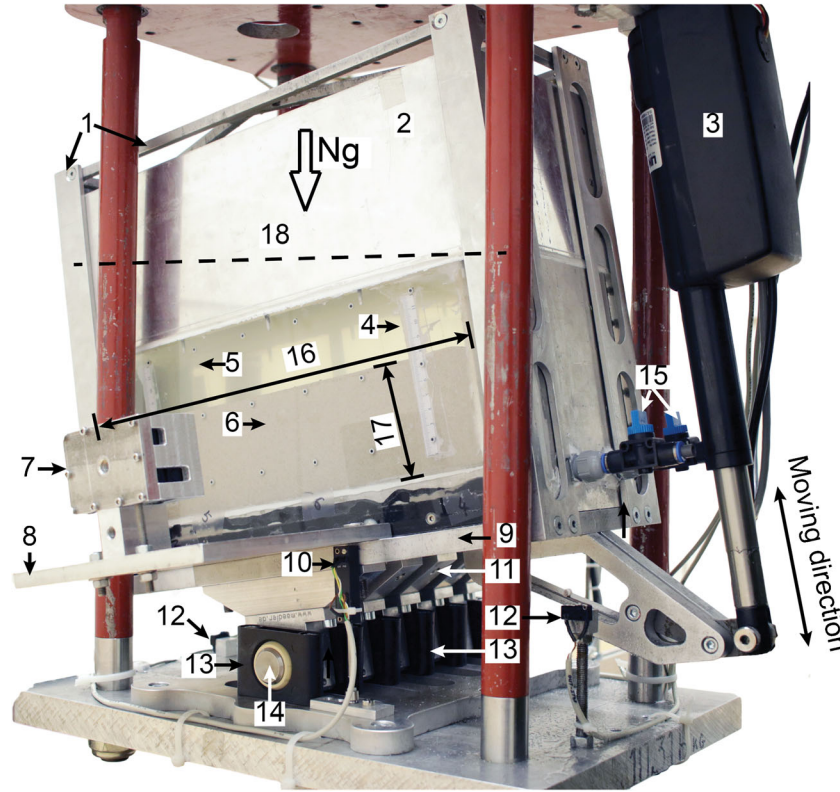


Fig. 11 Test set-up in the centrifuge carrier (model scale): 1, outer frame; 2, extension box; 3, linear motor; 4, scale; 5, fluid; 6, submerged sand; 7, high resolution, high speed camera; 8, camera holder; 9, base plate; 10, linear potentiometer; 11, bearing blocks; 12, switches; 13, shaft blocks; 14, rotation axis; 15, valves; 16, sample length: 355 mm; 17, sample height: 87 mm; 18, fluid table (it is initially parallel to the sample bottom with a distance of 180 mm)

0.002 %/s at model scale; the corresponding tilting rates at prototype will be N times smaller than that at model scale as explained in the next section.

Scaling law

Scaling law for tilting rate

In a centrifuge test, the scale factor for acceleration (a) is $a_r = a_p/a_m = 1/N$, where henceforward the subscripts p, m and r indicate prototype, model and the ratio of prototype to model, respectively; furthermore, the scale factor for length (L) is $L_r = L_p/L_m = N$. Therefore, considering the unit of acceleration, the scale factor for kinematic time (t_r^k) is:

$$t^k = \sqrt{\frac{L}{a}}, t_r^k = \frac{t_p^k}{t_m^k} = \sqrt{\frac{L_p a_m}{a_p L_m}} = N \quad (4)$$

where the superscript k refers to kinematic. Tilting rate has a unit of degree per second. The scale factor for slope angle is unity. Hence, the scale factor for tilting rate is:

$$TR_r = \frac{TR_p}{TR_m} = 1/t_r^k = 1/N \quad (5)$$

Scaling laws for pore fluid viscosity for static liquefaction

Based on Darcy's law, the specific discharge (q) can be expressed in the form of Eq. 6, where q has a unit of meter/second, K is hydraulic conductivity (as shown in Eq. 7) which is also called coefficient of permeability with a unit of meter/second, i is hydraulic gradient (dimensionless), κ is intrinsic permeability (m^2) which depends on soil properties, μ is dynamic viscosity ($kg\ m^{-1}\ s^{-1}$), ν is kinematic viscosity (St), ρ_f is fluid density and γ_f is unit weight of fluid at which the permeability is measured (Zienkiewicz et al. 1999).

$$q = Ki \quad (6)$$

$$K = \frac{\kappa \gamma_f}{\mu}, \mu = \nu \rho_f \quad (7)$$

Macroscopic scale

It is widely accepted that, in a $1/N$ -time scaled model under Ng condition, the scale factors for K , i and q are 1, $1/N$ and $1/N$, respectively, if the same pore fluid and soil are used in the model and prototype (Cargill and Ko 1983; Arulanandan et al. 1988; Taylor 1995; Singh and Gupta 2000; Garnier et al. 2007). Hence, the scale factor for seepage time (t_s^s) is N^2 as shown in Eq. 8 (Schofield 1980; Taylor 1995), where the superscript s refers to seepage. Due to the conflict between

the scaling laws for kinematic time (Eq. 4) and seepage time (Eq. 8), a pore fluid which is N times more viscous than water is recommended (e.g. Schofield 1980; Taylor 1995; Dewoolkar et al. 1999). The viscous fluid makes the ratio of kinematic time to seepage time in the prototype equals to that in the model, as explained in the Eqs. 9 and 10.

$$t^s = \frac{L}{q}, t_r^s = L_r/q_r = N^2 \quad (8)$$

$$\frac{\mu_p}{\mu_m} = \frac{1}{N} \rightarrow \frac{K_p}{K_m} = N \rightarrow \frac{q_p}{q_m} = 1 \rightarrow \frac{t_p^s}{t_m^s} = N \quad (9)$$

$$\frac{t_p^k}{t_m^k} = \frac{t_p^s}{t_m^s} \text{ or } t_r^k = t_r^s \left(\text{when } \frac{\mu_p}{\mu_m} = \frac{1}{N} \right) \quad (10)$$

Grain scale

Take et al. (2004) proposed that soil collapse initiates the sudden increase of pore pressure, which can be the triggering mechanism of static liquefaction. They mentioned that the duration of the generation of excess pore pressure can be a function of falling distance of a grain on to another one (h) and acceleration as expressed in Eq. 11, where the superscripts gen and grain stand for generation and grain scale, respectively. The scaling factor for length related factors is 1 at grain scale (Askarinejad et al. 2014).

$$t^{\text{gen.grain}} \propto \sqrt{\frac{h}{a}}, t_r^{\text{gen.grain}} = \sqrt{\frac{1}{a_r}} = \sqrt{N}. \quad (11)$$

Askarinejad et al. (2014) believe that the initial soil voids collapse should happen locally and hence the grain scale is of interest in the case of static liquefaction. They argue that the generation time of excess pore pressure due to the collapse of soil structure is \sqrt{N} times slower than its dissipation time at grain scale under Ng acceleration (see Eq. 11). Therefore, a fluid which is \sqrt{N} times more viscous than water as the pore fluid for a test at Ng is recommended so that the time for excess pore pressure generation and that for excess pore pressure dissipation are both scaled with the same factor as explained in Eqs. 12 and 13.

$$\frac{\mu_p}{\mu_m} = \frac{1}{\sqrt{N}} \rightarrow \frac{K_p}{K_m} = \sqrt{N} \rightarrow \frac{q_p}{q_m} = \frac{1}{\sqrt{N}} \rightarrow \frac{t_p^{\text{s.grain}}}{t_m^{\text{s.grain}}} = \sqrt{N} \quad (12)$$

$$t_r^{\text{gen.grain}} = t_r^{\text{s.grain}} \left(\text{when } \frac{\mu_p}{\mu_m} = \frac{1}{\sqrt{N}} \right) \quad (13)$$

Therefore, based on the scaling laws for pore fluid at grain scale, a submerging fluid with a viscosity of $\sqrt{10}$ should be used for a test under 10g condition. Hence, HPMC powder was used in this study to make the viscosity of the submerging fluid to be 3.2 cSt. The permeability of the sample with the viscous fluid was 3.2 times less than 4.2×10^{-5} m/s, i.e. 1.3×10^{-5} m/s (Table 1).

Furthermore, in order to investigate fluid viscosity effect on the sample, de-aired water as the submerging fluid was also applied.

Results and discussion

The landslides were triggered by tilting the sand layers gradually. To investigate the effects of the steepening rate of slope on slope instability, four tilting rates, namely 0.01, 0.05, 0.1 and 0.2°/s at prototype scale, were tested at 10g. The tilting started around 1200 s (prototype scale) after achieving the target g-level. No change in pore pressure was noticed before tilting, i.e. the consolidation due to the increase in g-level had finished. The characteristics of the tests are summarized in Table 2.

Coriolis effect on very loose sample during increasing of g-level

Due to the high sensitivity of the very loose sand samples, the standard increment rate of the angular velocity of the geo-centrifuge at TU Delft, which takes 67 s from 1g to 10g, could cause a local liquefaction (Fig. 12). This disturbance could happen due to the Coriolis effect. Hence, a very low increasing rate of centrifugal acceleration was adopted for all the tests listed in Table 2, which would take 990 s from 1g to 10g and could provide a gradual and smooth increase of hydrostatic pressure during the process of rising g-level.

The Coriolis acceleration (a_{Coriolis}) depends on the centrifuge angular velocity (ω) and the sample velocity in the centrifuge rotation plane (v_{rotation}), as described in Eq. 14 (Schofield 1980), where R_{ac} , R_{beam} and R_{sample} in Eq. 15 are the centrifuge rotation radius, length of centrifuge beam and the distance between the hinge of the centrifuge carrier and 1/3 of the sample height, respectively, and β is position angle indicating the rotation of the centrifuge carrier. During the development of ω , centrifuge acceleration (a_c) rises and the sample position changes with increasing β as illustrated in Fig. 13 and Eq. 16. In this process, soil sample moves in the centrifuge rotation plane; hence, it has a certain velocity in the centrifuge rotation plane v_{rotation} which can be expressed using Eq. 17. The changing rate of β (Eq. 18) can be obtained from Eqs. 15 and 16.

Figure 12 demonstrates that the maximum value of a_{Coriolis}/a_c is about 7.8% when the centrifuge takes 67 s from 1g to 10g and it is around 1% when the centrifuge takes 990 s from 1g to 10g. Hysteresis upon the local liquefaction was observed. Taylor (1995) proposed that Coriolis effects could be negligible when the ratio of Coriolis acceleration to centrifuge acceleration is less than 10% for dynamic modelling in centrifuge. However, this limit needs to be lowered for testing a saturated loose sand sample with D_r in the range of 20–30%. It is found that 1% is a reasonable value as the limit of a_{Coriolis}/a_c in this case.

$$\frac{a_{\text{Coriolis}}}{a_c} = \frac{2\omega v_{\text{rotation}}}{\omega^2 R_{\text{ac}}} \quad (14)$$

$$R_{\text{ac}} = R_{\text{beam}} + R_{\text{sample}} \sin \beta \quad (15)$$

$$\beta = \tan^{-1} \left(\frac{\omega^2 R_{\text{ac}}}{g} \right) \quad (16)$$

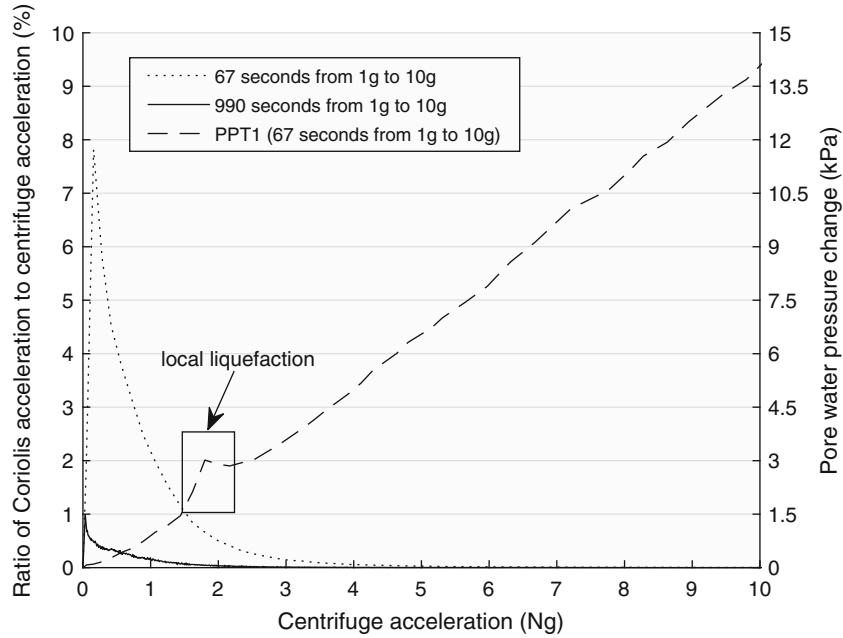


Fig. 12 Ratio of Coriolis acceleration to centrifuge acceleration and partial liquefaction during increasing of g-level

$$v_{\text{rotation}} = \frac{d(R_{\text{sample}} \sin \beta)}{dt} = R_{\text{sample}} \cos \beta \frac{d\beta}{dt} \quad (17)$$

$$\frac{d\beta}{dt} = \frac{2\omega R_{ac} \frac{d\omega}{dt}}{g + \omega^4 R_{ac}^2 / g - \omega^2 R_{\text{sample}} \cos \beta} \quad (18)$$

Sample failure

A high resolution (3840 × 2160 pixels), high speed camera (the highest frame rate is 30 fps) was used to take videos during all tests. The camera was connected to the tilting device with the camera holder (Fig. 11). Thus, it could rotate together with the strongbox. The captured videos (30 fps) show that the slope failures happened almost without any visible precursor. Figure 14 illustrates three frames at three tilting angles (θ), namely 0° , 17.0° and 17.7° , for test V_o.01_10g (Table 2). There was no local or global movement that could be detected during tilting before the liquefaction. The videos indicate that the liquefaction happened over the entire length and around 85% depth of the sample.

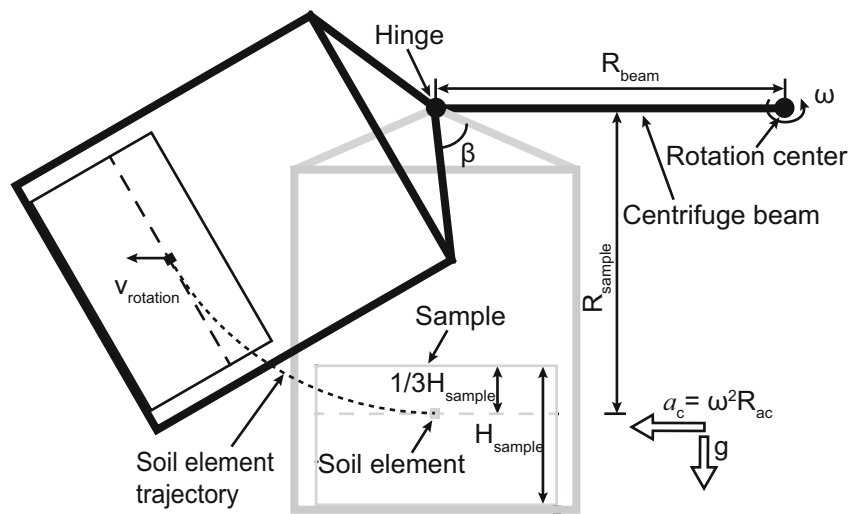
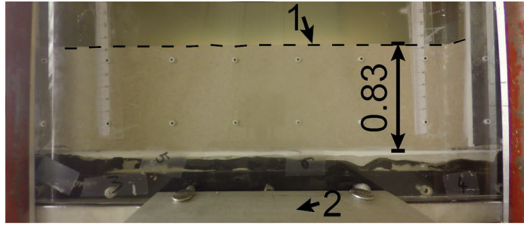
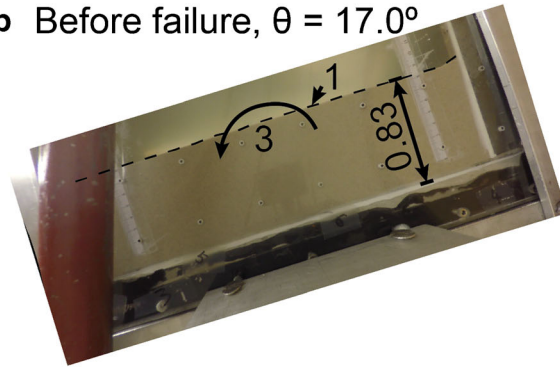


Fig. 13 Schematic description of sample moving velocity in the centrifuge rotation plane during the process of increasing centrifuge acceleration (grey, initial position when $\omega = 0$; black, position due to a certain amount of ω)

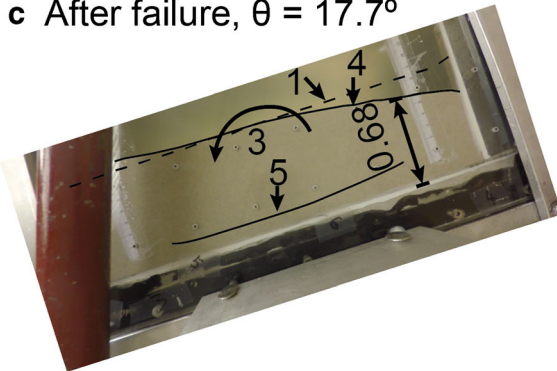
a Before tilting, $\theta = 0^\circ$



b Before failure, $\theta = 17.0^\circ$



c After failure, $\theta = 17.7^\circ$



d Schematic view of sample during tilting

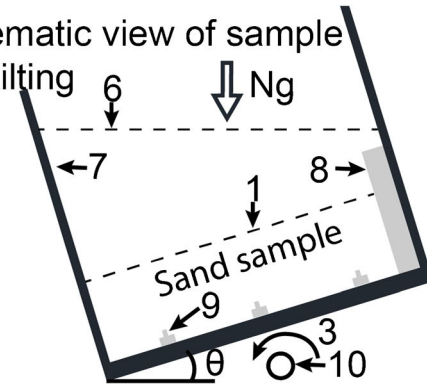


Fig. 14 Three frames of V_0.01_10g (unit: m, prototype scale): 1, sand surface before tilting/failure; 2, camera holder; 3, tilting direction; 4, sand surface after failure; 5, observed failure surface; 6, water table; 7, strongbox; 8, PVC block; 9, PPTs (from left to right: PPT1, PPT2 and PPT3); 10, rotation axis

Due to the fact that excess pore pressure dissipated during the liquefaction, the sliding sand stopped when the excess pore pressure reduced to zero. It should be noted that boundary effects would be expected from the low end of the strongbox which would prohibit moving of liquefied sand. It is expected that a larger scale in length would give a gentler after failure (De Groot et al. 2019). Considering that W_0.01_10g and W_0.1_10g did not fail up to the maximum tilting angle of the set-up (20°) while all other tests failed before reaching the limitation (Table 2), it can be concluded that the boundary effects play an important role in the post-failure behaviour of flow slides but barely influence the samples before the onset of liquefaction. Since this paper mainly focuses on investigating the triggering mechanism of static liquefaction, we believe that the boundary effects are of minor importance before the onset of static liquefaction.

Failure angle

The failure angles for centrifuge tests are demonstrated in Fig. 15 with respect to tilting rate at prototype scale. The tilting rate effect on slope instability can be revealed by comparing the failure angles in slopes with the same viscous fluid (Fig. 15). A reduction in failure angle is visible with increasing tilting rate. This is also observed from results of 10g tests with water as failure occurred in W_0.2_10g but not happened in W_0.1_10g and W_0.01_10g. The generation and dissipation of pore pressure coexist when a fully saturated sand sample is under shearing (Iverson 1993; Taylor 1995; Goren et al. 2010). It is reasonable to assume that the dependency of slope instability on tilting rate is related to the difference

between the pore pressure generation rate and the pore pressure dissipation rate. A faster increase of the slope angle increases the probability of occurrence of micro-collapses in the soil body and hence triggers the switch of drainage condition from drained to undrained then causes the generation of excess pore pressure and liquefaction.

The tilting mechanism applied in the centrifuge tests mimics the rise of seabed slope angle as result of scouring/dredging. Therefore, the development of stress state for a soil element in the samples is similar to that of a soil element which lies below a seabed slope with gradually increasing inclination as shown in Fig. 1. The tilting rate effect, i.e. slope angle changing rate ($\dot{\theta}$) effect, is expressed in Fig. 16. For a test with a higher tilting rate, the sample was stable before arriving at point B₁ with a failure angle of θ_{f1} , and then the stress state follows path 1 till to full liquefaction at point C; for a test with a lower tilting rate, the stress path continues further under drained condition to point B₂ with a failure angle of θ_{f2} ($> \theta_{f1}$) following by the path 2 under undrained condition. It can be inferred that the instability line is a function of shear rate as demonstrated in Fig. 16.

This postulation can also explain the two tests performed by De Jager (2018) in the Liquefaction Tank as shown in Table 4. Test1, with a tilting rate of 0.12°/s, failed at a slope angle of 6.1°, while Test2, with a tilting rate of 0.01°/s, did not fail even at a slope angle of 10° (the maximum tilting angle of 1g liquefaction tank). Test1 and V_0.1_10g have similar tilting rate, while the slope failure angles for these two tests are different (i.e. 6.1° for Test1 and 11.5° for V_0.1_10g). It is believed that the difference in the relative

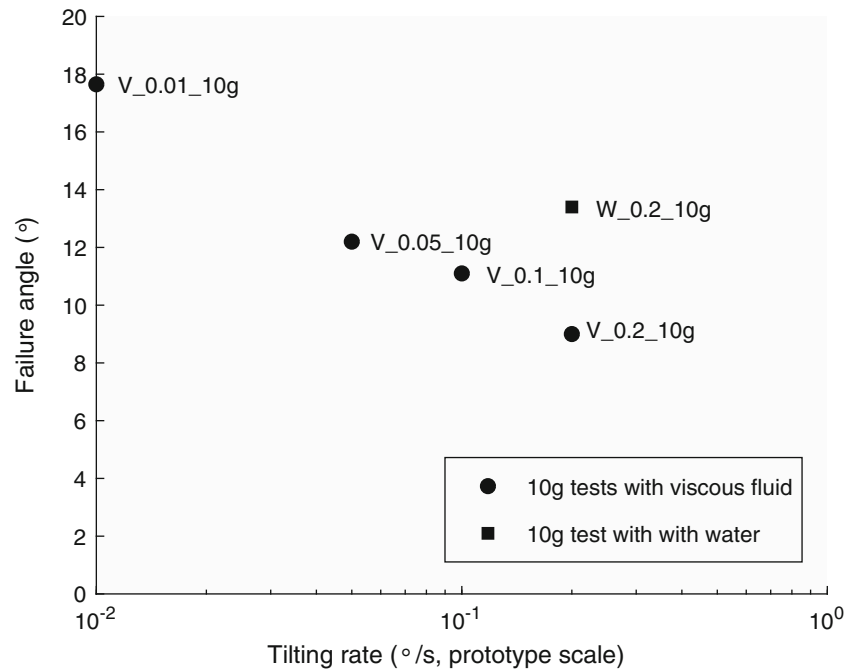


Fig. 15 Tilting rate effect on slope failure angles for 10g tests

densities of these two tests (i.e. 35.0% for Test1 and 41.0% for V_0.1_10g) is the main reason for the difference in the failure angles (Askarinejad et al. 2019).

It can be found that fluid viscosity plays an important role in triggering static liquefaction as well. W_0.2_10g failed at a larger slope angle than V_0.2_10g (the failure angles for W_0.2_10g and V_0.2_10g are 13.4° and 9.9°, respectively), and W_0.1_10g and W_0.01_10g did not fail but V_0.1_10g and V_0.01_10g failed. The pore fluid viscosity of the tests with viscous fluid is 3.2 times higher than that for the tests with water. Therefore, the possible generated pore pressure for the tests with water dissipates 3.2 times faster than that for the tests with viscous fluid. Dewoolkar et al. (1999) discovered a similar behaviour from results of level

ground seismic centrifuge tests. By giving the same earthquake motion, the sample submerged by viscous fluid liquefied, while the sample submerged by water did not.

Excess pore pressure due to static liquefaction

Static liquefaction of submerged loose sand layer is related to sudden development of pore fluid pressure which reduce effective stresses under undrained condition. Therefore, knowing the behaviour of pore fluid pressure during the increase of slope angle is important to evaluate the sand behaviour. Pore fluid pressures are measured using three pore pressure transducers (PPT1, PPT2 and PPT3) located at sample bottom as illustrated in Fig. 2 and Fig. 14.

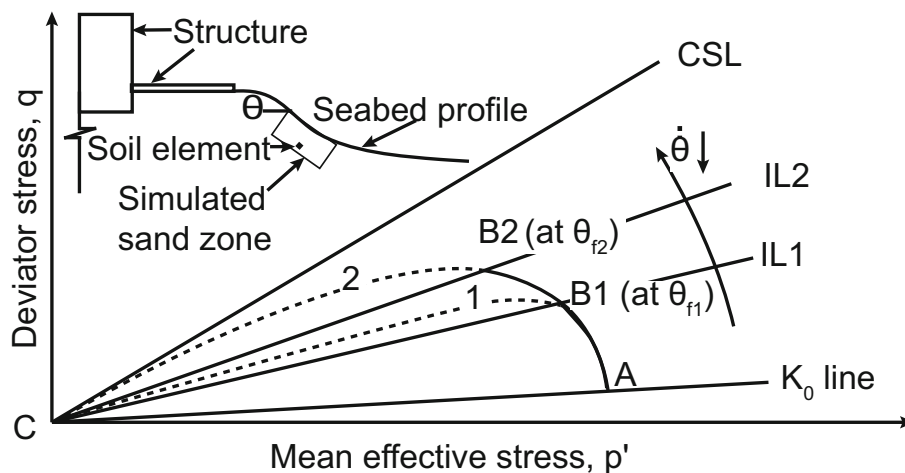


Fig. 16 Dependency of static liquefaction triggering mechanism on slope angle changing rate

Table 4 Two tests performed by De Jager (2018) in the 1g liquefaction tank

Test name	Tilting rate (°/s)	D_r (%)	Failure angle (°)	Sand layer height (m)
Test1	0.12	35.0	6.1	0.51
Test2	0.01	35.9	No failure ^a	0.51

^a The maximum tilting angle for the 1g liquefaction tank is 10°

Figure 17 demonstrates the pore fluid pressure change for tests V_0.01_10g_NoSand and V_0.01_10g taking to the pore fluid pressure before the tilting as zero. V_0.01_10g_NoSand was performed with viscous fluid only but no sand. During tilting, the slope angle increased, as shown in Fig. 14; however, the fluid table remained perpendicular to the direction of the resultant centrifuge acceleration. Therefore, the distance between the fluid surface and each PPT changed according to the tilting angle. As a result of increasing fluid table near slope toe, the hydrostatic fluid pressure of PPT1 increased, i.e. positive values as illustrated in Fig. 17. PPT3 shows the opposite change since it was situated at slope crest side. The hydrostatic fluid pressure of PPT2 dropped less than that of PPT3 as it was close to the middle of the sample (see Fig. 2). Moreover, the transient build-up of pore pressures indicates the static liquefaction for V_0.01_10g. The moment at which the pore pressure starts to increase is defined as the moment of failure.

The difference between the pore fluid pressures from tests with sand (V_0.2_10g, V_0.1_10g, V_0.05_10g and V_0.01_10g) and the hydrostatic fluid pressures from V_0.01_10g_NoSand gives the change of excess pore pressure as shown in Fig. 18. The transient increase in excess pore pressures was detected in all the four tests. Due to the fact that the data logging rate was one sample per 5 s at prototype scale (two samples per second at model scale), details of the development of pore pressures were not completely recorded especially for V_0.2_10g which has the

highest tilting rate (see Fig. 18a). Assuming the transient excess pore pressures increased and decreased linearly around their summits, the maximum excess pore pressures can be taken as the intersection of growing segment and declining segment of the transient excess pore pressures, for instance, the estimated peak for PPT1 in Fig. 18a.

For tests V_0.2_10g and V_0.1_10g, PPT3 detected a faster variation in pore pressure than PPT1 and PPT2 which can be seen in around 5 s (prototype scale) before the failures. While after failure, the pore pressures recorded by PPT1 and PPT2 increased faster than that recorded by PPT3 before reaching the peaks. It implies that a local part of the samples failed firstly and then caused the liquefaction. This local area should be closer to PPT3 (near slope crest during the change in slope angle) than the other two sensors. Positive excess pore pressures were observed in tests V_0.2_10g to V_0.05_10g, while, in contrast, slight negative excess pore pressures were detected in test V_0.01_10g before failure. It can be inferred that a faster changing rate of the slope angle (V_0.2_10g to V_0.05_10g) would result in a faster growth of shear stress in the loose sand layer, hence a quicker increase in excess pore pressure due to the contraction of sand layer. The negative excess pore pressures for V_0.01_10g indicate that dilation was happening at the bottom layer of the sample before the failure; however, the side images captured during this test show that the top loose layer of the sample failed first and the liquefied zone propagated quickly toward the lower levels of this sample.

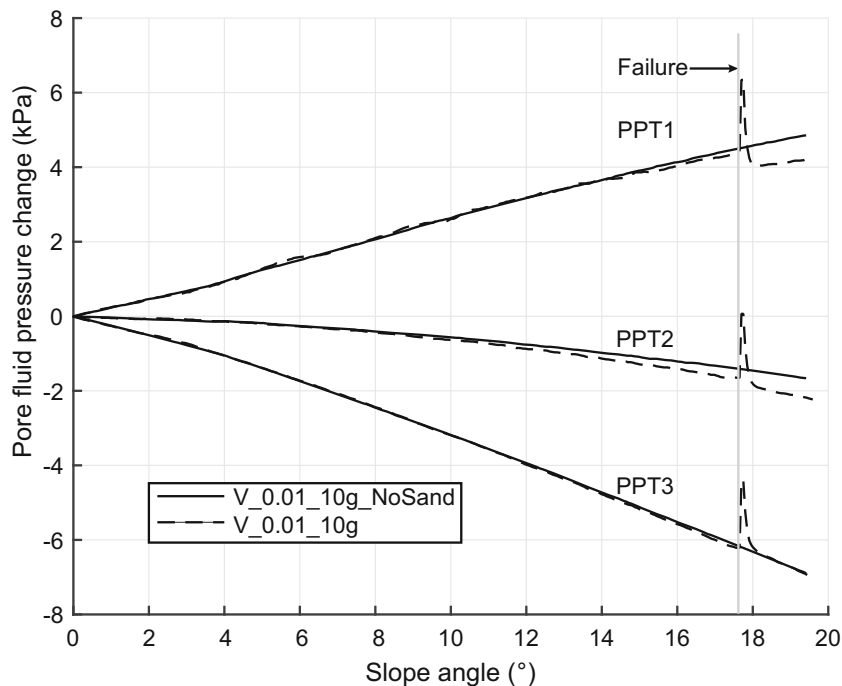


Fig. 17 Pore pressure change with increasing slope angle for tests V_0.01_10g_NoSand and V_0.01_10g

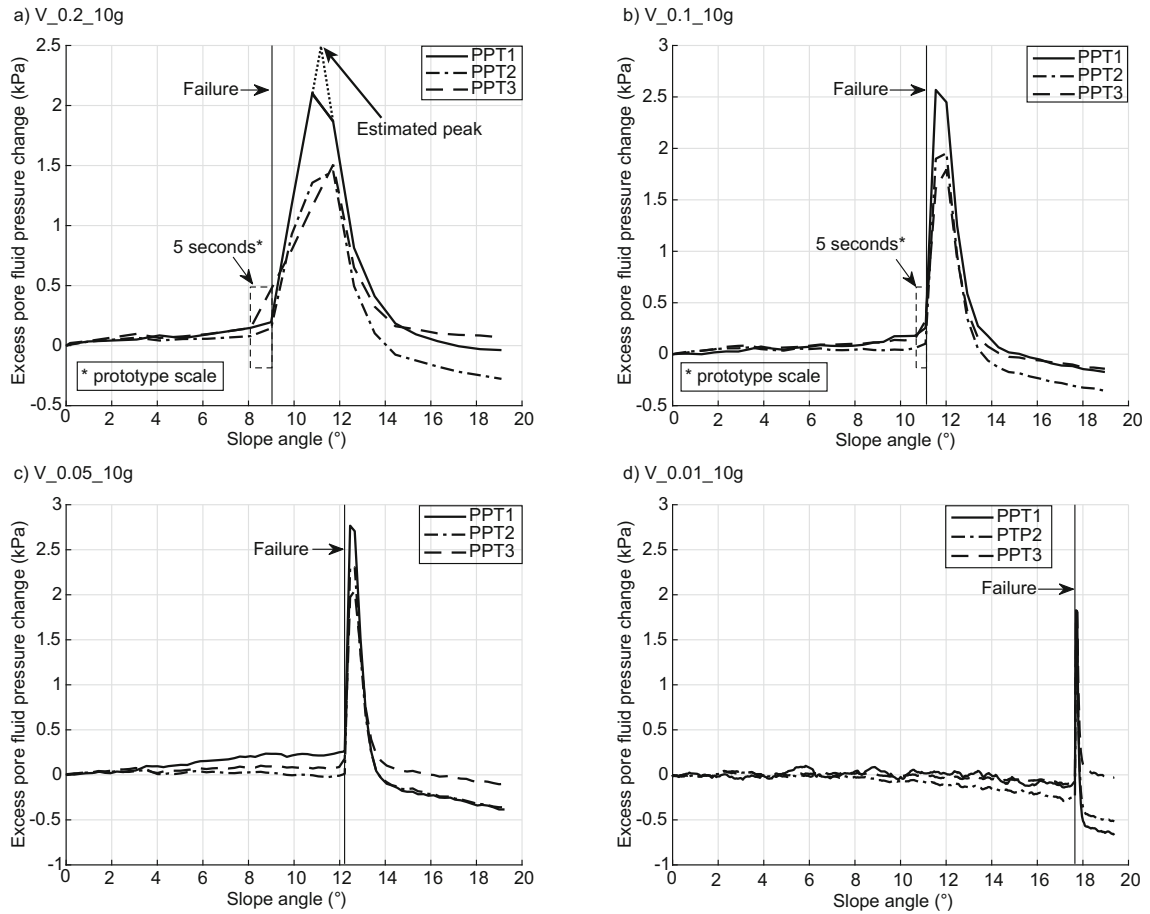


Fig. 18 Excess pore pressure with increasing slope angle for 10 g tests with viscous fluid

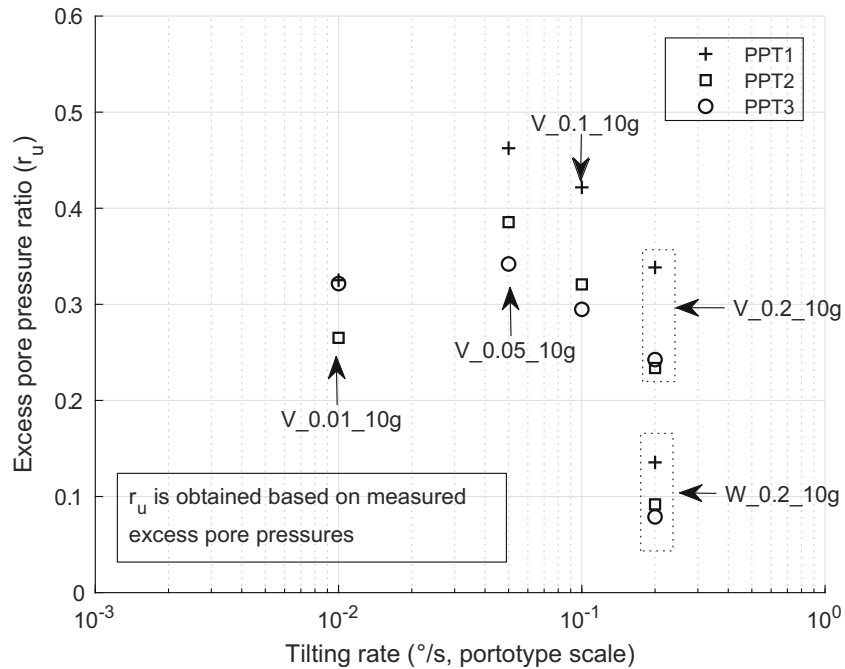


Fig. 19 Excess pore pressure ratios for all 10g tests with static liquefaction

Excess pore pressure ratio

The excess pore pressure ratio for a soil element inside a submerged infinite slope can be defined using Eq. 19 (Biondi et al. 2000),

$$r_u = \frac{u}{\sigma_v} = \frac{u}{\gamma' H \cos^2 \theta_f} \quad (19)$$

where u is measured excess pore pressure, γ' is buoyancy unit weight, H is normal distance between slope surface and the soil element, and θ_f is slope angle (at failure). The excess pore pressure ratios (r_u) for the centrifuge tests with liquefaction are demonstrated in Fig. 19. The excess pore pressure distribution was very much influenced by the dynamic motion of the liquefied mass during slope failures, i.e. affected by the post-failure behaviour. Hence the excess pore pressure ratio at the position of PPT1 (near slope toe) is the highest and that of PPT3 (near slope crest) is the lowest among the three PPTs (see Fig. 2).

According to the definition of r_u (Eq. 19), $r_u = 1$ would be expected when liquefaction happens. However, all the obtained r_u values are less than 1 in this study. This might be explained by the following two facts: firstly, only around 85% of the depth of the samples failed during slope liquefaction whereas the PPTs were located at sample bottom. Since generation and dissipation coexist during flow slides, the excess pore pressure measured by the sensor is less than that in the sliding soil mass; secondly, the real maximum excess pore pressures might not be recorded by the PPTs due to the relatively low data logging rate as explained in Fig. 18a.

Summary and conclusions

In this study, the performance of a newly developed strongbox with an integrated fluidization system for preparing very loose, fully saturated and uniform sand samples is discussed. Moreover, the details of a novel set-up made for simulating triggering mechanisms of submarine landslides in a beam centrifuge have been illustrated. The soil properties of the samples have been examined using computed tomography technique. The tilting rate effects have been investigated by testing samples at various slope steepening rates under 10g condition. Static liquefaction has been observed at various slope angles. Submerging fluid has been prepared based on the scaling law for pore fluid flow at grain scale. The main conclusions are presented below:

- The fluidization technique can be applied to prepare samples for centrifuge models. This technique could make reproducible, very loose and uniform fully saturated samples directly on the beam centrifuge carrier ruling out any disturbance which could be caused by sample transportation. Less effort is needed compared to the traditional techniques such as dry pluviation, moist tamping, drizzle and wet pluviation methods.
- Statically liquefied submarine landslides can be triggered in centrifuge condition by the tilting technique. This technique is similar to the natural process of slopes over-steepening due to scouring erosion or dredging activities.
- Tilting rate (or slope overstepping rate) affects the generation of pore pressure, hence governs the slope instability regime. The instability line is a function of slope increasing rate, i.e. shearing rate.
- A statically liquefied submarine landslide happens in a very short time with no visible precursors long before the failure.

- Coriolis effect during starting of centrifuge should be taken into account for testing loose saturated sample. A value of 1% for the ratio of Coriolis acceleration to centrifuge acceleration is suggested.

Acknowledgements

The authors are grateful to Simon Gerlach, Han J. de Visser, Kees van Beek, Ronald van Leeuwen, Leon Roessen, Bert Bakker, P.M. Meijvogel-de Koning and Tom Philips for their technical input to this study.

Funding information

The first author is financially supported by China Scholarship Council.

Open Access This article is distributed under the terms of the Creative Commons Attribution 4.0 International License (<http://creativecommons.org/licenses/by/4.0/>), which permits unrestricted use, distribution, and reproduction in any medium, provided you give appropriate credit to the original author(s) and the source, provide a link to the Creative Commons license, and indicate if changes were made.

References

- Acosta EA, Tibana S, Soares de Almeida MS, Saboya F Jr (2017) Centrifuge modeling of hydroplaning in submarine slopes. *Ocean Eng* 129:451–458. <https://doi.org/10.1016/j.oceaneng.2016.10.047>
- Andresen A, Bjerrum L (1967) Slides in subaqueous slopes in loose sand and silt. In: Richards AF (ed) *Marine geotechnique*. University of Illinois Press, pp 221–239
- Arulanandan K, Thompson PY, Kutter BL, Meegoda NJ, Muraleetharan KK, Yogachandran C (1988) Centrifuge modeling of transport processes for pollutants in soils. *J Geotech Eng* 114(2):185–205. [https://doi.org/10.1061/\(ASCE\)0733-9410\(1988\)114:2\(185\)](https://doi.org/10.1061/(ASCE)0733-9410(1988)114:2(185))
- Askarinejad A, Beck A, Springman SM (2014) Scaling law of static liquefaction mechanism in geocentrifuge and corresponding hydromechanical characterization of an unsaturated silty sand having a viscous pore fluid. *Can Geotech J* 52(6):708–720. <https://doi.org/10.1139/cgj-2014-0237>
- Askarinejad A, Zhang W, de Boorder M and van der Zon J (2018) Centrifuge and numerical modelling of static liquefaction of fine sandy slopes. In: McNamara A, Divall S, Goodey R, Taylor N, Stallebrass S and Panchal J (eds) *Physical modelling in geotechnics*, CRC Press, pp 1119–1124
- Askarinejad A, Zhang W and Maghsoudloo A (2019) Physical modelling of static liquefaction of seabed due to scouring. Paper presented at The XVII European Conference on Soil Mechanics and Geotechnical Engineering (ECSMGE-2019), Reykjavik Iceland, 1–6 September
- Biondi G, Cascone E, Maugeri M, Motta E (2000) Seismic response of saturated cohesionless slopes. *Soil Dyn Earthq Eng* 20(1–4):209–215. [https://doi.org/10.1016/S0267-7261\(00\)00051-8](https://doi.org/10.1016/S0267-7261(00)00051-8)
- Bjerrum L (1971) Subaqueous slope failures in Norwegian fjords. In: *Proceedings of the First International Conference on Port and Ocean Engineering Under Arctic Conditions*. vol 1. pp 24–47
- Boylan N, Gaudin C, White D and Randolph M (2010) Modelling of submarine slides in the geotechnical centrifuge. In: Springman SM et al (eds) *Physical modelling in geotechnics (ICPMG 2010)*, vol 2. CRC Press, Zurich, Switzerland, pp 1095–1100
- Byrne P, Puebla H, Chan D, Soroush A, Morgenstern N, Cathro D, Gu W, Phillips R, Robertson P and Hofmann B (2000) CANLEX full-scale experiment and modelling. *Can Geotech J* 37(3):543–562. <https://doi.org/10.1139/t00-042>
- Cargill KW, Ko H-Y (1983) Centrifugal modeling of transient water flow. *J Geotech Eng* 109(4):536–555. [https://doi.org/10.1061/\(ASCE\)0733-9410\(1983\)109:4\(536\)](https://doi.org/10.1061/(ASCE)0733-9410(1983)109:4(536))
- Chapuis RP (2004) Permeability tests in rigid-wall permeameters: determining the degree of saturation, its evolution, and its influence of test results. *Geotech Test J* 27(3):304–313. <https://doi.org/10.1520/GTJ10905>
- Coulter S, Phillips R (2003) Simulating submarine slope instability initiation using centrifuge model testing. In: J. L et al. (ed) *Submarine mass movements and their consequences*, vol 19. Springer, Dordrecht, pp 29–36. https://doi.org/10.1007/978-94-010-0093-2_4

- De Groot M, Lindenberg J, Mastbergen DR and Van den Ham GA (2012) Large scale sand liquefaction flow slide tests revisited. Paper presented at the Eurofuge 2012, Delft, The Netherlands, pp 1–22
- De Groot M, Lindenberg J, Mastbergen DR and Van den Ham GA (2019) Liquefaction flow slides in large flumes. *International Journal of Physical Modelling in Geotechnics* 19: 37–53. <https://doi.org/10.1680/jpmg.16.00026>
- De Jager RR, Maghsoudloo A, Askarinejad A and Molenkamp F (2017) Preliminary results of instrumented laboratory flow slides. In: Rohe A et al. (eds) *Proceedings of the 1st International Conference on the Material Point Method (MPM 2017)*, vol 175. Elsevier, Delft, The Netherlands, pp 212–219. <https://doi.org/10.1016/j.proeng.2017.01.012>
- De Jager RR (2018) *Assessing liquefaction flow slides: beyond empiricism*. Dissertation, Delft University of Technology
- Della N, Arab A, Belkhatir M (2011) Influence of specimen-reconstituting method on the undrained response of loose granular soil under static loading. *Acta Mech Sinica* 27(5):796–802. <https://doi.org/10.1007/s10409-011-0462-8>
- Dewoolkar MM, Ko H-Y, Stadler AT and Astaneh S (1999) A substitute pore fluid for seismic centrifuge modeling. *Geotech Test J* 22(3):196–210. <https://doi.org/10.1520/GTJ11111J>
- Elgamal A, Yang Z, Lai T, Kutter BL, Wilson DW (2005) Dynamic response of saturated dense sand in laminated centrifuge container. *J Geotech Geoenviron* 131(5):598–609. [https://doi.org/10.1061/\(ASCE\)1090-0241\(2005\)131:5\(598\)](https://doi.org/10.1061/(ASCE)1090-0241(2005)131:5(598))
- Garnier J, Gaudin C, Springman SM, Culligan PJ, Goodings D, König D, Kutter B, Phillips R, Randolph MF, Thorel L (2007) Catalogue of scaling laws and similitude questions in geotechnical centrifuge modelling. *Int J Phys Model Geotechnics* 7(3):1–23
- Goren L, Aharonov E, Sparks D, Toussaint R (2010) Pore pressure evolution in deforming granular material: a general formulation and the infinitely stiff approximation. *J Geophys Res Solid Earth* 115(B9). <https://doi.org/10.1029/2009JB007191>
- Gu R, Dogandžić A (2016) Blind X-ray CT image reconstruction from polychromatic Poisson measurements. *IEEE Trans Comput Imaging* 2(2):150–165. <https://doi.org/10.1109/TCI.2016.2523431>
- Gue C, Soga K, Bolton M and Thusyanthan N (2010) Centrifuge modelling of submarine landslide flows. In: Springman SM et al (eds) *Physical modelling in geotechnics (ICPMG 2010)*, vol 2. CRC Press, Zurich, Switzerland, pp 1113–1118
- Gupta LP, Tanikawa W, Hamada Y, Hirose T, Ahagon N, Sugihara T, Abe N, Nomura S, Masaki Y, Wu HY, Lin W, Kinoshita M, Yamada Y (2018) Examination of gas hydrate-bearing deep ocean sediments by X-ray computed tomography and verification of physical property measurements of sediments. *Mar Pet Geol*. <https://doi.org/10.1016/j.marpetgeo.2018.05.033>
- Higo Y, Oka F, Kimoto S, Sanagawa T and Matsushima Y (2011) Study of strain localization and microstructural changes in partially saturated sand during triaxial tests using microfocus X-ray CT. *Soils Found* 51(1):95–111. <https://doi.org/10.3208/sandf.51.95>
- Ilstad T, Marr JG, Elverhøi A, Harbitz CB (2004) Laboratory studies of subaqueous debris flows by measurements of pore-fluid pressure and total stress. *Mar Geol* 213(1–4):403–414. <https://doi.org/10.1016/j.margeo.2004.10.016>
- Iverson RM (1993) Differential equations governing slip-induced pore-pressure fluctuations in a water-saturated granular medium. *Math Geol* 25(8):1027–1048. <https://doi.org/10.1007/BF00911548>
- Ko H (1994) Modeling seismic problems in centrifuges. In: Leung CF et al (eds) *Centrifuge 94: proceedings of the International Conference Centrifuge 94*. Balkema, Rotterdam, pp 3–12
- Kraft LM Jr, Gavin TM, Bruton JC (1992) Submarine flow slide in Puget Sound. *J Geotech Eng* 118(10):1577–1591. [https://doi.org/10.1061/\(ASCE\)0733-9410\(1992\)118:10\(1577\)](https://doi.org/10.1061/(ASCE)0733-9410(1992)118:10(1577))
- Kramer S (1988) Triggering of liquefaction flow slides in coastal soil deposits. *Eng Geol* 26(1):17–31. [https://doi.org/10.1016/0013-7952\(88\)90004-X](https://doi.org/10.1016/0013-7952(88)90004-X)
- Kvalstad T, Nadim F and Arbiz C (2001) Deepwater geohazards: geotechnical concerns and solutions. Paper presented at the Offshore Technology Conference, Houston, Texas. <https://doi.org/10.4043/12958-MS>
- Kyriakou Y, Meyer E, Prell D, Kachelrieß M (2010) Empirical beam hardening correction (EBHC) for CT. *Med Phys* 37(10):5179–5187. <https://doi.org/10.1118/1.3477088>
- Lade PV (1992) Static instability and liquefaction of loose fine sandy slopes. *J Geotech Eng* 118(1):51–71. [https://doi.org/10.1061/\(ASCE\)0733-9410\(1992\)118:1\(51\)](https://doi.org/10.1061/(ASCE)0733-9410(1992)118:1(51))
- Lade PV, Yamamoto JA (2011) Evaluation of static liquefaction potential of silty sand slopes. *Can Geotech J* 48(2):247–264
- Lowe DR (1976) Subaqueous liquefied and fluidized sediment flows and their deposits. *Sedimentology* 23(3):285–308. <https://doi.org/10.1111/j.1365-3091.1976.tb00051.x>
- Maghsoudloo A, Galavi V, Hicks MA and Askarinejad A (2017) Finite element simulation of static liquefaction of submerged sand slopes using a multilaminar model. In: 19th International Conference on Soil Mechanics and Geotechnical Engineering, vol 2. Seoul, South Korea, pp 801–804
- Maghsoudloo A, Askarinejad A, R.R. DJ, Molenkamp F and Hicks M (2018) Experimental investigation of pore pressure and acceleration development in static liquefaction induced failures in submerged slopes. Paper presented at the 9th International Conference of Physical Modelling in Geotechnics, London, pp 987–992
- Petrovic A, Siebert J and Rieke P (1982) Soil bulk density analysis in three dimensions by computed tomographic scanning. *Soil Sci Soc Am J* 46(3):445–450. <https://doi.org/10.2136/sssaj1982.03615995004600030001x>
- Phillips R, Byrne P (1995) Modeling flowslides caused by static loading. *Transp Res Rec*:12–21
- Rietdijk J, Schenkeveld F, Schaminée P and Bezuijen A (2010) The drizzle method for sand sample preparation. In: Springman SM et al (eds) *Physical modelling in geotechnics (ICPMG 2010)*, vol 1. CRC Press, Zurich, Switzerland, pp 267–272
- Sadrekarami A (2016) Static liquefaction analysis considering principal stress directions and anisotropy. *Geotech Geol Eng* 34(4):1135–1154. <https://doi.org/10.1007/s10706-016-0033-7>
- Sassa S, Sekiguchi H (1999) Wave-induced liquefaction of beds of sand in a centrifuge. *Geotechnique* 49(5):621–638. <https://doi.org/10.1680/geot.1999.49.5.621>
- Schofield AN (1980) Cambridge geotechnical centrifuge operations. *Geotechnique* 30(3):227–268. <https://doi.org/10.1680/geot.1980.30.3.227>
- Silvis F, Md G (1995) Flow slides in the Netherlands: experience and engineering practice. *Can Geotech J* 32(6):1086–1092. <https://doi.org/10.1139/t95-107>
- Singh DN, Gupta AK (2000) Modelling hydraulic conductivity in a small centrifuge. *Can Geotech J* 37(5):1150–1155. <https://doi.org/10.1139/t00-027>
- Sladen J, D'hollander R and Krahn J (1985a) The liquefaction of sands, a collapse surface approach. *Can Geotech J* 22(4):564–578. <https://doi.org/10.1139/t85-076>
- Sladen J, D'hollander R, Krahn J and Mitchell D (1985b) Back analysis of the Nerlerk berm liquefaction slides. *Can Geotech J* 22(4):579–588. <https://doi.org/10.1139/t85-077>
- Spence K, Guymer I (1997) Small-scale laboratory flowslides. *Geotechnique* 47(5):915–932. <https://doi.org/10.1680/geot.1997.47.5.915>
- Stewart DP, Chen Y-R and Kutter BL (1998) Experience with the use of methylcellulose as a viscous pore fluid in centrifuge models. *Geotech Test J* 21(4):365–369. <https://doi.org/10.1520/GTJ11376J>
- Take WA, Bolton MD, Wong PCP, Yeung FJ (2004) Evaluation of landslide triggering mechanisms in model fill slopes. *Landslides* 1(3):173–184
- Taylor R (1995) *Geotechnical centrifuge technology*. Blackie Academic & Professional, Chapman & Hall, London
- The Dow Chemical Company (2002) *METHOCEL cellulose ethers: Technical handbook*. http://msdssearch.dow.com/PublishedLiteratureDOWCOM/dh_096d/0901b8038096d9ff.pdf?filepath=/pdfs/noreg/192-01062.pdf&fromPage=GetDoc. Accessed September 2002
- Vaid YP, Sivathayalan S and Stedman D (1999) Influence of specimen-reconstituting method on the undrained response of sand. *Geotech Test J* 22(3):187–195. <https://doi.org/10.1520/GTJ11110J>
- Wanatowski D, Chu J (2012) Factors affecting pre-failure instability of sand under plane-strain conditions. *Geotechnique* 62(2):121–135. <https://doi.org/10.1680/geot.9.P.111>
- Wen C, Yu Y (1966) A generalized method for predicting the minimum fluidization velocity. *AIChE J* 12(3):610–612
- Wood DM (2014) *Geotechnical modelling*. CRC Press, London
- Yamada Y, Yamashita Y, Yamamoto Y (2010) Submarine landslides at subduction margins: insights from physical models. *Tectonophysics* 484(1–4):156–167. <https://doi.org/10.1016/j.tecto.2009.09.007>
- Yin M, Rui Y, Xue Y (2017) Centrifuge study on the runout distance of submarine debris flows. *Mar Georesour Geotechnol*:1–11. <https://doi.org/10.1080/1064119X.2017.1411407>
- Zhang J, Lin H and Wang K (2015) Centrifuge modeling and analysis of submarine landslides triggered by elevated pore pressure. *Ocean Eng* 109:419–429. <https://doi.org/10.1016/j.oceaneng.2015.09.020>
- Zienkiewicz OC, Chan A, Pastor M, Schrefler B and Shiomi T (1999) *Computational geomechanics*. John Wiley & Sons, Chichester, New York, Weinheim, Brisbane, Singapore, Toronto

Electronic supplementary material The online version of this article (<https://doi.org/10.1007/s10346-019-01200-z>) contains supplementary material, which is available to authorized users.

W. Zhang · A. Askarinejad (✉)

Faculty of Civil Engineering and Geosciences,
TU Delft,
Delft, The Netherlands
Email: A.Askarinejad@tudelft.nl

W. Zhang

e-mail: w.zhang-3@tudelft.nl